Journal Name

ARTICLE

Facile Preparation of β-/γ-MgH_2 Nanocomposites under Mild Conditions and Pathways to Rapid Dehydrogenation

Received 00th January 20xx,
Accepted 00th January 20xx

DOI: 10.1039/x0xx00000x

www.rsc.org/

Xuezhang Xiao,[a,b] Zhe Liu,[a] Sina Saremi Yarahmadi,[a] Duncan H. Gregory[a*]

A magnesium hydride composite with enhanced hydrogen desorption kinetics can be synthesized *via* a simple wet chemical route by ball milling MgH_2 with LiCl as an additive at room temperature followed by tetrahydrofuran (THF) treatment under an Ar atmosphere. The as-synthesized composite comprises *ca*. 18 mass% orthorhombic γ-MgH_2 and 80 mass% tetragonal β-MgH_2 as submicron-sized particles. The β-/γ-MgH_2 nanocomposite exhibits a dehydrogenation capacity of 6.6 wt.% and starts to release hydrogen at ~260 °C; *ca*. 140 °C lower than that of commercial MgH_2. The apparent activation energy for dehydrogenation is 115±3 kJ mol^{-1}, which is *ca*. 46 % lower than that of commercial MgH_2. Analysis suggests that the meta-stable γ-MgH_2 component either directly dehydrogenates exothermically or first transforms into stable β-MgH_2 very close to the dehydrogenation onset. The improved hydrogen release performance can be attributed both to the existence of the MgH_2 nanostructure and to the presence of γ-MgH_2.

1. Introduction

Hydrogen is a promising alternative energy carrier, which can facilitate the transition from fossil fuels to clean energy. Among several tangible advantages are a high energy density, its availability from multiple sources (potentially sustainably) and its utilisation with zero carbon emissions. Implementing a safe, low cost, and fully reversible solid hydrogen storage material with a gravimetric capacity in excess of 7.5 wt.% is major challenge for developing next generation energy storage systems.[1, 2] Magnesium is a strong candidate material for solid state hydrogen storage because of its excellent reversibility, earth abundance, low cost and high hydrogen storage capacity (7.6 wt.%). It has thus been the topic of extensive research over the last 50 years.[3, 4] However, the stable phase of magnesium hydride (β-MgH_2) possesses a rutile structure with strong Mg-H bond. The ensuing large decomposition enthalpy of 75 kJ mol^{-1} H_2 results in relatively high desorption temperatures (>300 °C) coupled with a slow hydrogen diffusion rate, limiting its practical applications.[5] Different approaches such as catalysis,[6, 7] alloying,[8, 9] composite formation[10, 11] and nanostructuring[12-14] have been employed to improve the hydrogen uptake/release kinetics and thermodynamics of MgH_2. One of the most widely used strategies is to reduce the MgH_2 particle size by mechanical ball milling, hence lowering the activation energy of desorption. Moreover, the use of transition metals (such as Ti, V, Co, Ni, Pd, Al), intermetallic compounds and transition metal oxides, halides and hydrides as additives/catalysts can improve the (de)hydriding kinetics of the Mg-H system.[15-19] However, since such additives add to the mass of the material, the hydrogen storage capacity is reduced, sometimes considerably.

Recent theoretical calculations and experimental results show that the high-pressure meta-stable γ-MgH_2 phase exhibits improved dehydrogenation kinetics compared to that of the room temperature/pressure phase, β-MgH_2.[20-23] However, it should be noted that full transformation of β-MgH_2 to γ-MgH_2 has not been successfully achieved previously. γ-MgH_2 is usually produced using extreme processing conditions requiring high pressure (2.5–8 GPa) and high temperature (250–900 °C) or *via* ultra-high energy reactive ball milling under *ca*. 80-150 bar H_2 with a Ti-based catalyst.[21, 22, 24, 25] Moreover, a fundamental understanding of the formation and decomposition mechanisms of meta-stable γ-MgH_2 is still lacking.

In the present work, we combined a mechanical ball milling process with THF treatment to prepare a β-/γ-MgH_2 "nanocomposite" without the need for high (hydrogen) pressure or high temperature. Subsequent studies reveal the likely role of the γ-phase and the γ-β phase transition in the dehydrogenation of nanostructured β-/γ-MgH_2 as compared with β-MgH_2 itself.

2. Experimental Section

All manipulations were carried out under inert atmosphere in an Argon-filled Saffron Scientific recirculating glovebox (< 10 ppm O_2 and H_2O). MgH_2 (Sigma-Aldrich, 98 %) and LiCl (Sigma-Aldrich, ≥99.9 %) were used as received. Approximately 0.5 g

a WestCHEM, School of Chemistry, Joseph Black Building, University of Glasgow, Glasgow G12 8QQ Scotland, UK. E-mail address: Duncan.Gregory@glasgow.ac.uk (D.H.Gregory). Tel.: +44 (0)141 330 6438; Fax: +44 (0)141 330 4888

b School of Materials Science and Engineering, Zhejiang University, Hangzhou 310027, China. E-mail address: xzxiao@zju.edu.cn (X.Z. Xiao). Tel./fax: +86 (0)571 8795 1876.

of MgH_2/LiCl (1:1 molar ratio) was ball milled for 4 h at 400 rpm with a ball-to-powder ratio of 40:1 under 1 bar Ar atmosphere using a Retsch PM100 planetary ball mill. Then, the black ball-milled MgH_2/LiCl mixture was washed with tetrahydrofuran (THF) to remove LiCl using centrifugation. This process was repeated several times until a dark brown precipitate was observed. In addition, the precipitate was dried at room temperature under dynamic vacuum using a Schlenk line. For comparison, the as received MgH_2 was first pre-ball milled and then washed with THF and dried subsequently under the same conditions. Hereafter, the as received MgH_2 is denoted as **MgH_2-A**, the ball milled MgH_2 as **MgH_2-B**, the ball milled MgH_2/LiCl mixture as **MgH_2-C**, the ball milled MgH_2 after treatment with THF as **MgH_2-D**, and the ball milled MgH_2/LiCl mixture after treatment with THF as **MgH_2-E**.

The phase and structural characterisation of samples was performed by X-ray diffraction in glass capillaries (PXD; Bruker D8 Advance) over a 2θ range of 10-85° with a step size of 0.016° using Cu Kα radiation. Full profile structure refinement was performed for the **MgH_2-E** sample *via* the Rietveld method using the GSAS and EXPGUI software packages.[26, 27] Fourier Transform Infrared (FTIR) spectroscopy was conducted on ~1 mg solid samples using a Shimadzu 8400S spectrometer equipped with the *IR-solution* software package, scanning from *ca*. 500-4000 cm^{-1} with a resolution of 2 cm^{-1}. The solid state samples were measured by Attenuated Total Reflectance (ATR) by pressing the samples on to the diamond crystal of a MIRacle (PIKE) sample holder. Particle size and morphology were probed by scanning electron microscopy (SEM, H Carl-Zeiss Sigma V_p) with an accelerating potential of 10 kV. The samples for SEM were mounted on carbon tabs under an inert atmosphere and sputter coated with gold.

The dehydrogenation behaviour of all the samples was measured by simultaneous thermogravimetric-differential thermal analysis (TG-DTA; Netzsch STA 409 instrument contained within an Ar-filled MBraun UniLab recirculating glovebox with <0.1 ppm H_2O, 0.1 ppm O_2) coupled to a Hiden HPR20 mass spectrometer. Heating rates of 2, 5, 8 and 10 °C min^{-1} respectively were employed from room temperature to 450 °C under flowing Ar gas (≥99.999 % purity, 60 mL min^{-1}).

3. Results and discussion

PXD was performed in order to investigate the effects of ball milling and THF treatment on the structure and composition of the MgH_2 samples. Patterns of **MgH_2-A** (as-received MgH_2), **MgH_2-B** (ball-milled MgH_2) and MgH_2/LiCl mixtures before and after THF treatment (**MgH_2-C, -D, -E)** are shown in Fig. 1. As shown, the as-received hydride is composed mainly of *β*-MgH_2 along with a small amount of Mg (Fig. 1(a)). *β*-MgH_2 is still present as the main phase after ball milling in **MgH_2-B**, although possible minor traces of *γ*-MgH_2 can be detected in this sample and Mg reflections become subsumed into the broader *β*-MgH_2 peaks and increased background (Fig. 1(b)). Interestingly, the PXD peaks of *γ*-MgH_2 become slightly more prominent after THF treatment (**MgH_2-D**) as shown in Fig. 1(d). However, it should be noted that the intensities of the *γ*-MgH_2 diffraction peaks in **MgH_2-B** and **MgH_2-D** are weak compared to the *β*-MgH_2 reflections, suggesting that the conversion to the *γ*-phase is very limited in samples milled without additive. This is perhaps not surprising since *γ*-MgH_2 is a non-equilibrium, meta-stable phase. Its presence as a minor phase might be explained from two competing processes during ball milling: one promotes the formation of *γ*-MgH_2 *via* the mechanically (pressure) driven *β*→*γ* transformation, whereas the other favours the reverse, thermally driven *γ*→*β* transformation.[28]

The diffraction peaks of *β*-MgH_2 become broader and relatively weaker for **MgH_2-C**. Cl^- is the strongest X-ray scatterer in the sample and so LiCl dominates the powder pattern, but nevertheless the data indicate that ball-milling using LiCl can further decrease the particle size and potentially increase the concentration of crystal defects in MgH_2. LiCl has a high solubility in THF (1.14 mmol g^{-1})[29] and as expected, LiCl is completely removed after treating the MgH_2/LiCl mixture with the solvent. The **MgH_2-E** sample is composed of MgH_2 with Mg (presumably remaining from the original as-received material) present as a minor phase (Fig. 1(e)). Notably, the relative intensity of the *γ*-MgH_2 diffraction peaks increases after ball milling and treatment with THF. Other variations of the preparative process in which milled samples were mixed with LiCl without washing, washed with THF without adding LiCl or treated with both LiCl and THF, but milled for different times, all resulted in lower (or negligible) *γ*-MgH_2 content compared to **MgH_2-E** (ESI; Figure S1).

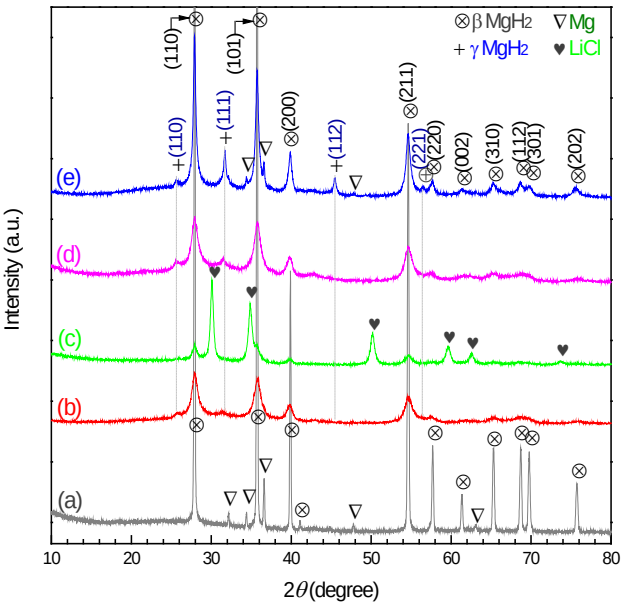

Fig. 1 PXD patterns of (a) **MgH_2-A**, (b) **MgH_2-B**, (c) **MgH_2-C**, (d) **MgH_2-D**, (e) **MgH_2-E** samples. For the definition of the sample labels, please see the accompanying text.

Rietveld refinement against PXD data was performed for **MgH_2-E** in order to obtain further information on the phase abundance and cell parameters of the ball-milled MgH_2/LiCl sample after THF treatment. The results are shown in Fig. 2 and Table 1. The quantitative analysis confirms that the **MgH_2-**

E sample is composed of two different polymorphs of MgH_2: 18 wt.% orthorhombic *γ*-MgH_2 (space group: *Pbcn*) and 80 wt.% tetragonal *β*-MgH_2 (space group: $P4_2/mnm$) (in addition to 2 wt.% Mg as minor phase). It is well known that the *γ*-MgH_2 is a high pressure non-equilibrium phase, which is commonly formed by the transformation of *β*-MgH_2 at high pressure (typically 2.5–8 GPa) and high temperature (250–900 °C) or by ultra-high energy reactive ball milling under H_2 pressure with a Ti-based catalyst for long durations.[22, 24, 25]

FTIR spectra were collected for **MgH_2-E** to provide further insight in our evaluation of the effect of THF treatment on the formation of the *β*-/*γ*-MgH_2 nanocomposites (Fig. 3). By means of comparison, the FTIR spectrum of **MgH_2-A** (commercial MgH_2) displays two broad Mg-H bands in the range of 1400-800 and 800-500 cm^{-1}.[30]

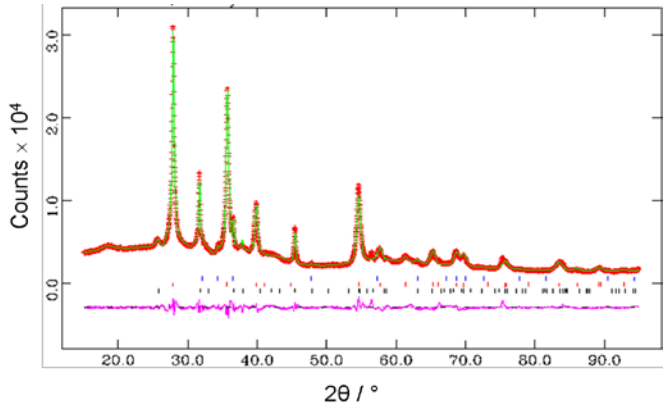

Fig. 2 Rietveld profile plot for **MgH_2-E**. Observed (crosses), calculated (solid line) and difference curves (bottom line) are shown. Vertical bars (|) correspond to Bragg positions for *γ*-MgH_2, *β*-MgH_2 and Mg phases respectively (from top to bottom).

Table 1 Selected crystallographic data obtained from the Rietveld refinement for **MgH_2-E**.

Radiation, wavelength / Å		X-ray, 1.5406	
Component phase	*γ*-MgH_2	β-MgH_2	Mg
Space group	*Pbcn*	$P4_2/mnm$	$P6_3/mmc$
Cell parameters / Å	*a*=4.440(1)	*a*=4.5111(3)	*a*=3.2073(4)
	b=5.409(1)	*c*=3.0162(2)	*c*=5.201(2)
	c=4.8804(5)		
Density, ρ_x / g cm^{-3}	1.492	1.424	1.742
Phase fraction / wt.%	18.0(5)	79.6(1)	2.4(1)
Observations, parameters		4831, 56	
R_{wp}, R_P		0.046, 0.034	

After 1 min of drying, most of the THF is still present in **MgH_2-E** as evidenced in the FTIR spectrum by the strong C-H stretching bands at 2853 and 2978 cm^{-1} and the very strong ring stretching and breathing bands (C-O and C-C) at *ca*. 909 and 1070 cm^{-1} (Fig 3(b)).[31] With the possible exception of the Mg-H bending band centred at ca. 650 cm^{-1}, bands from the hydride are not discernible in this sample given the presence of THF. After 10 min of drying (Fig 3(c)), the weakening of the THF bands observed above suggests that the solvent is almost completely removed from **MgH_2-E** while the broad Mg-H bands at 1400-800 and 800-500 cm^{-1} are clearly visible. It should be noted that the colour of the **MgH_2-E** sample turns from dark grey to dark brown after treating with THF. This colour remains after drying for 10 min indicating that some polymeric MgH_2·THF is still present.[32, 33] In the case of the 60 min drying, only broad MgH_2 signals remain (Fig 3(d)), suggesting the THF can be completely removed from the **MgH_2-E** sample after 60 min drying under dynamic vacuum. (We used the latter conditions as standard for the studies of **MgH_2-E.**) Combined with the PXD results in Fig. 1 and 2, it is suggested that the phase transformation process of MgH_2 nanocomposites takes place following reaction (1):

$$\beta\text{-}MgH_2\cdot THF \rightarrow \beta\text{-}/\gamma\text{-}MgH_2 + THF \quad (1)$$

Furthermore, as the drying process was performed, it was observed that MgH_2 powder was almost uniformly deposited on the inner wall of the Schlenk flask while water condensed and ice formed on the outer surface of the flask. These observations would be consistent with the endothermic vapourisation of THF under dynamic vacuum.

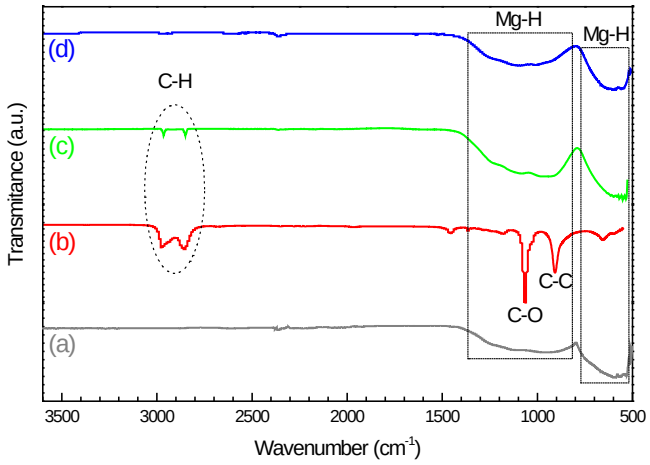

Fig. 3 The FTIR spectra of (a) **MgH_2-A** sample, (b) **MgH_2-E** sample dried for 1 min, (c) MgH_2-E sample dried for 10 min, and (d) MgH_2-E sample dried for 60 min.

While there are several reports of the synthesis of *γ*-MgH_2 under relatively high pressure and high temperature,[21-23] to the best of our knowledge, the meta-stable *γ*-phase has not been synthesized previously under such mild conditions as we observe here (ball milling with LiCl for 4 h under 1 bar Ar atmosphere and treating with THF at room temperature). Previously, the room temperature synthesis of 11 wt.% *γ*-MgH_2 (with the remainder of the hydride present as *β*-MgH_2) *via* hydrogenation of Mg in THF solution has been reported but this required a hydrogen gas pressure of 8 MPa for 1-2 days.[21] From this previous evidence and our own, we propose that the THF solution (and likely formation of the polymeric hydride THF adduct) plays a vital role in the synthesis of the meta-stable *γ*-MgH_2 phase. The formation of *γ*-MgH_2 under mild conditions therefore must be attributable to a combination of ball mill-induced nanostructuring using LiCl together with the THF treatment of the milled hydride material.

Particle size, distribution and the morphology of **MgH_2-A**, **MgH_2-B**, and **MgH_2-E** samples before dehydrogenation were

characterized using SEM as shown in Fig. 4. Commercial MgH_2 (**MgH_2-A**) is composed of some laminar structures ranging from 20-150 µm across. In the **MgH_2-B** sample, the particle size is significantly reduced and ranges from 80-800 nm with an average particle size of ~300 nm due to the agglomeration of the irregular particles that occurs following milling. Interestingly, after ball milling with LiCl as an additive and THF treatment (**MgH_2-E**), a lamellar microstructure predominates with particle lengths/widths ranging from 50-400 nm and particle thicknesses of the order of 10 nm (Fig 4(c,d)). Moreover, it is apparent that the surfaces of the layer structures in the **MgH_2-E** sample have a high asperity, which would be expected to lead to an increase in specific surface area compared to the smooth particle surfaces in the **MgH_2-B** sample (i.e. ball milled without LiCl). Although agglomeration seems more severe after THF treatment, such a surface morphology in **MgH_2-E** is anticipated to lead to a high concentration of surface defects and coupled with the nanoscaling effects of milling, could enhance diffusion and hence enhance the hydrogen absorption/desorption kinetics.[33]

Fig. 5 shows the TG-DTA curves of the **MgH_2-A-E** samples. The evolved gas mass spectrum from **MgH_2-E** is presented in Fig. 6. The desorption temperature of commercial MgH_2 peaks above 400 °C, which is in agreement with previous reports.[21] The weight loss for **MgH_2-A** (*ca*. 7.0 wt.%) is slightly lower than the theoretical value, which is due to the Mg impurity present in the commercial sample. Compared with commercial MgH_2, both the desorption temperatures and kinetics of **MgH_2-B** and **MgH_2-C** are improved because of the reduction in particle size following ball milling. **MgH_2-C** exhibited the lowest desorption peak temperature of 306.5 °C. This stems from the fact that the fine **MgH_2-C** particles were prepared using LiCl as an additive, which should act as a milling aid, further reducing the particle size.[34] It is widely accepted that the smaller the MgH_2 particles, the faster the desorption kinetics and the lower the desorption temperature.[13] However, the experimental gravimetric hydrogen capacity on desorption is reduced from 6.89 wt.% for **MgH_2-B** to 2.57 wt.% for **MgH_2-C**, due to the additional mass of "inactive" LiCl in the **MgH_2-C** sample.

With respect to the DTA curve of **MgH_2-D**, a *ca*. 20 °C increase in dehydriding peak temperature was observed compared to that of **MgH_2-B**. A comparable increase in peak temperature occurs between **MgH_2-C** and **MgH_2-E**. In both cases the differences probably originate from the increased particle agglomeration following THF treatment. It should be emphasized, however, that the hydrogen desorption onset temperature of **MgH_2-D** is *ca*. 25 °C lower than that of **MgH_2-B**, as is clear from the TG curves. Even more remarkably, the onset of hydrogen desorption for **MgH_2-E** decreases to *ca*. 260 °C, which is almost 150 °C lower than that for commercial MgH_2 (**MgH_2-A**). Moreover, **MgH_2-E** exhibits a mass loss of 6.6 wt.%. Although this is slightly lower than the theoretical value for dehydrogenation of MgH_2, importantly no other impurity gases (such as THF, HCl, CO or CO_2) were observed in the mass spectrum (Fig. 6). Of particular note, is a weak exothermic peak at ~290 °C that occurs in the DTA profile of **MgH_2-E** before the stronger endothermic signal at ~337 °C (Fig. 5(e)). One possible explanation for this exothermic peak is the phase transformation from meta-stable γ-MgH_2 to the more stable β-phase.[35] A similar phase transformation phenomenon was also reported in the AlH_3 system, where γ-AlH_3 transforms into the α-phase as an exothermic process.[36] Careful comparison of the DTA profiles additionally suggests that a weaker endothermic event overlaps with the exothermic peak at *ca*. 300 °C and merges with the stronger endothermic peak at *ca*. 337 °C. This coincides with a weight loss of *ca*. 1.16 wt.% in the TG profile for **MgH_2-E** (Fig 5). This weight loss at lower temperature presumably corresponds to the decomposition of a fraction of smaller size β-MgH_2 particles[22] that either originate from milling with LiCl (as seen for **MgH_2-C**) or are generated *in situ* from γ-MgH_2 (following the exothermic phase transition). The second, strong endothermic peak at ~337 °C in the DTA profile of **MgH_2-E** thus results from the dehydrogenation of β-MgH_2. Therefore, the improved dehydrogenation characteristics of **MgH_2-E** could be attributed to the formation of a nanocomposite containing meta-stable γ-MgH_2 as engineered by combining ball milling and THF treatments.

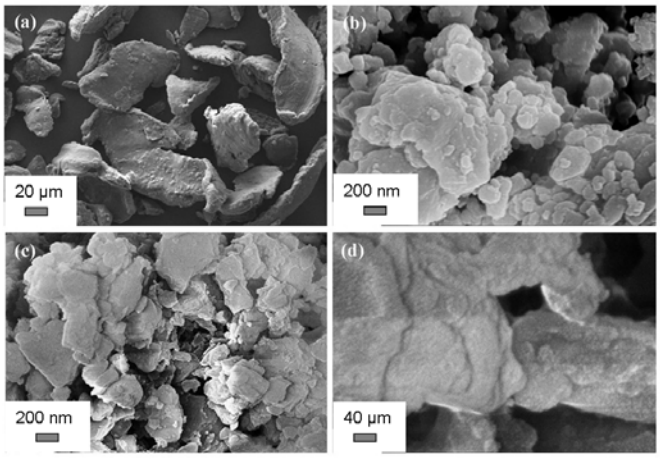

Fig. 4 SEM images of (a) **MgH_2-A**, (b) **MgH_2-B**, (c) and (d) **MgH_2-E** samples before dehydrogenation.

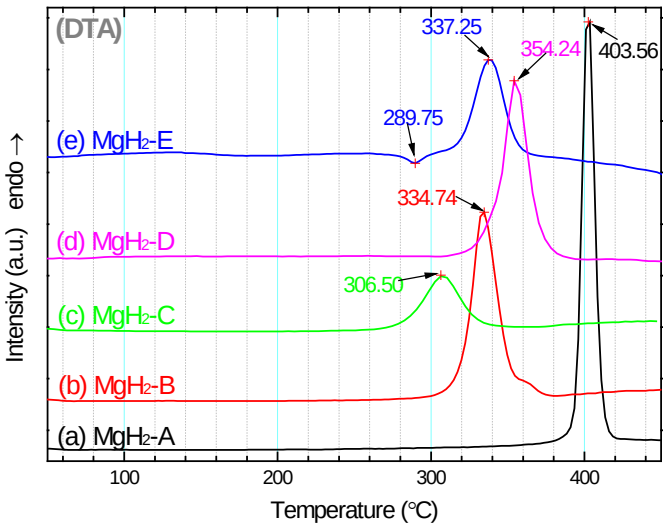

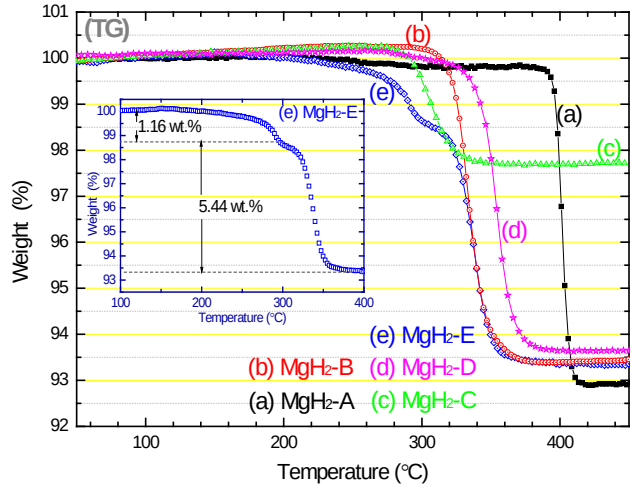

Fig. 5 TG-DTA curves of (a) **MgH_2-A**, (b) **MgH_2-B**, (c) **MgH_2-C**, (d) **MgH_2-D**, and (e) **MgH_2-E** samples. The heating rate was 2 °C min^{-1} from room temperature to 450 °C in each case. The inset shows the detail of the mass loss profile for **MgH_2-E**.

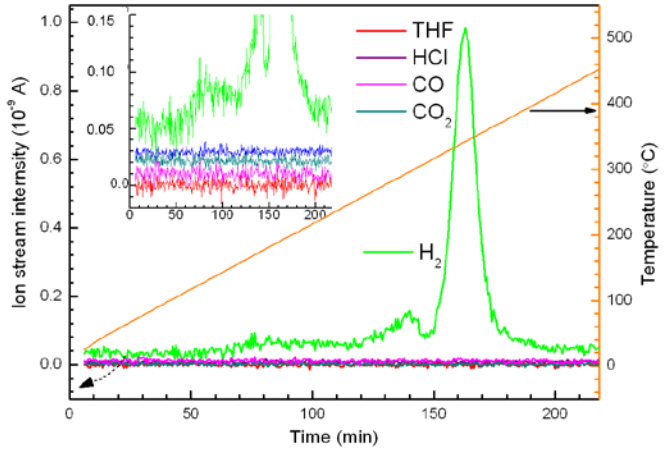

Fig. 6 Evolved gas mass spectrum from **MgH_2-E**. The inset compares the signal from H_2 to those for other potential evolved gases. (The heating rate was 2 °C min^{-1} from room temperature to 450 °C.)

In a bid to understand the dehydrogenation pathway of the *β-/γ*-MgH_2 nanocomposite, we performed a series of *ex-situ* PXD experiments sampled from the system at different temperatures during dehydrogenation. Fig. 7 presents the *ex-situ* PXD patterns from the dehydrogenation of **MgH_2-E** at five selected temperature points. Prior to the heating process, **MgH_2-E** is composed of *β*-MgH_2, *γ*-MgH_2 and Mg. On heating to 200 °C (Fig. 7(b)), the intensity of the *γ*-MgH_2 diffraction peaks increases coupled with a reduction in peak width due to the improved crystallinity of the phase. As the temperature is increased to 310 °C (Fig. 7(c)), the diffraction peaks of the meta-stable *γ*-MgH_2 phase disappear completely and the *β*-MgH_2 diffraction peaks dominate the pattern. Moreover, upon further increase of the temperature to 350 °C, the intensity of the *β*-MgH_2 reflections gradually diminish, while the Mg peaks intensify. Additional heating to 450 °C leads to the formation of the Mg as the major phase and the complete absence of *β*-MgH_2. A small amount of MgO is also detected in the patterns, possibly originating from a surface layer of oxide on particles of the as-supplied MgH_2,[28] or arising from handling of the samples during the diffraction experiments. Taking the TG-DTA data (Fig. 5) into account, the weight loss (1.16 wt.% H_2) at 300 °C is ~17.6 % of the total hydrogen gravimetric desorption capacity measured for **MgH_2-E** (6.6 wt.% H_2). This figure (17.6 %) is very close to the *γ*-MgH_2 phase fraction of 18.0(5) wt.% derived from Rietveld analysis of the *β-/γ*-MgH_2 nanocomposite. Although from the data available it is not possible to determine definitively whether the *γ*-MgH_2 phase dehydrogenates directly to Mg (equation 2) or first transforms to *β*-MgH_2 prior to hydrogen release (equation 3), there is little doubt that the lower temperature hydrogen release is elicited by the presence of the *γ*-MgH_2 in the hydride mixture.

$$x\,(\gamma\text{-}MgH_2) + (1\text{-}x)(\beta\text{-}MgH_2) \rightarrow x\,Mg + (1\text{-}x)\beta\text{-}MgH_2 + xH_2 \rightarrow Mg + H_2 \quad (2)$$

$$x\,(\gamma\text{-}MgH_2) + (1\text{-}x)(\beta\text{-}MgH_2) \rightarrow \beta\text{-}MgH_2 \rightarrow Mg + H_2 \quad (3)$$

A similar *γ→β* phase transformation event has already been proposed from *in situ* PXD experiments in the MgH_2 system.[35] We suggest that the release of heat from an exothermic *γ→β* transition could provide the means by which dehydrogenation occurs more easily in the *β-/γ*-MgH_2 nanocomposite. Ultimately, a detailed dehydrogenation pathway for *γ*-MgH_2 is not yet known and thermodynamic data for the *γ*-phase is also not available. Simultaneous *in situ* powder diffraction combined with TGA could provide the best means for elucidating the dehydrogenation mechanism of this *β-/γ*-MgH_2 nanocomposite in the future.

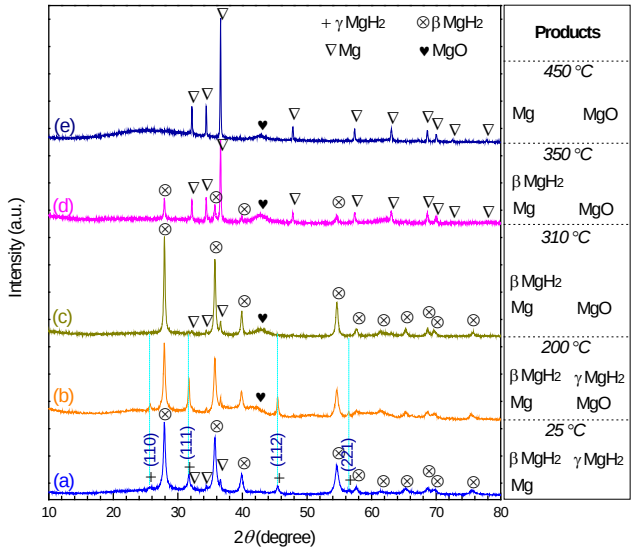

Fig. 7 *Ex*-situ PXD patterns of **MgH_2-E** sample at different dehydrogenation stages. (a) before dehydrogenation, (b) dehydrogenated at 200 °C, (c) dehydrogenated at 310 °C, (b) dehydrogenated at 350 °C, (c) dehydrogenated at 450 °C

In order to gain a better insight into how the MgH_2 dehydrogenation kinetics might have been improved as a result of nanocomposite formation, the apparent activation energies (E_a) for dehydrogenation for **MgH_2-A, MgH_2-B** and

MgH_2-E were quantitatively determined *via* the Kissinger method, *viz*.[37]

$$\ln(\delta/T_p^2) = -E_a/RT_p + \ln(AR/E_a) \quad (5)$$

Where δ is the heating rate, T_p is the absolute temperature at the maximum desorption rate (desorption peak temperature), A is the pre-exponential factor and R is the gas constant. In this work, T_p was obtained using DTA with heating rates of 2, 5, 8, and 10 °C min^{-1} respectively. The salient details of the DTA profiles for samples **MgH_2-A, MgH_2-B** and **MgH_2-E** are displayed in Fig. 8 and the dependence of $\ln(\delta/T_p^2)$ *vs*. $1/T_p$ is shown in Fig. 9. The intrinsic linearity of the curves indicates that the hydrogen desorption kinetics of MgH_2 follows the non-isothermal Kissinger equation and comprises a first order decomposition reaction.[37] The E_a was calculated from the slope ($-E_a/R$) of the fitted line, as shown in Fig. 9. The E_a for **MgH_2-E** is calculated to be 115±3 kJ mol^{-1}, which is ~46 % lower than that of commercial MgH_2 (213±6 kJ mol^{-1}) and ~17 % lower than MgH_2 that is ball milled only (138±6 kJ mol^{-1}). This result suggests that the nanostructuring of the *β-/γ*-MgH_2 composite may lower the driving force for Mg nucleation, resulting in enhanced kinetics and a reduced dehydrogenation temperature without the need for catalysts or additives.[38]

The as-synthesized *β-/γ*-MgH_2 nanocomposite offers a capacity of 6.6 wt.% H_2 and superior hydrogen desorption kinetics without the requirement of a catalyst. However, from our preliminary experiments, the re-/dehydrogenation properties of the nanocomposite on cycling are not clear. Given the presence of the exothermic step in the initial hydrogen release, one might expect that the advantages of the *β-/γ*-phase behaviour are lost in subsequent cycles unless the material undergoes further processing. Additional experiments are underway to investigate the reversibility of the hydrogen absorption and desorption in the *β-/γ*-MgH_2 nanocomposite system and the feasibility of a catalytic strategy to improve performance and cyclability still further.

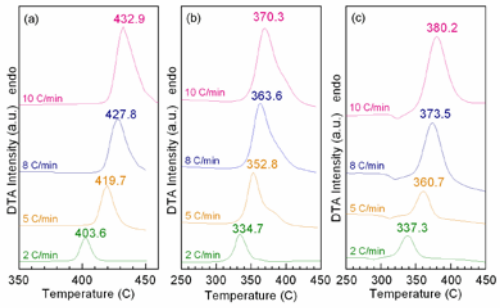

Fig. 8 DTA curves of (a) **MgH_2-A**, (b) **MgH_2-B** and (c) **MgH_2-E** samples at different heating rates.

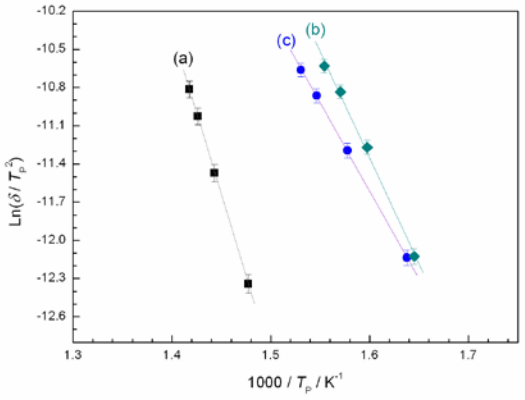

Fig. 9 Kissinger plots for the dehydrogenation of (a) **MgH_2-A** (commercial MgH_2); (b) **MgH_2-B** and (c) **MgH_2-E**.

4. Conclusions

In summary, an MgH_2 nanocomposite composed of tetragonal *β*-MgH_2 and 18 % orthorhombic *γ*-MgH_2 has been prepared for the first time without recourse to high pressure or temperature. By optimizing the ball milling conditions, addition of LiCl and use of THF solvent, the *β-/γ*-MgH_2 nanocomposite so-produced is capable of releasing 6.6 wt.% H_2 with rapid kinetics, from *ca*. 260 °C without the use of a catalyst. The apparent activation energy for dehydrogenation of the *β-/γ*-MgH_2 nanocomposite is calculated to be 115±3 kJ mol^{-1}, which is almost half that of commercial MgH_2 (213±6 kJ mol^{-1}). PXD, FTIR and SEM analyses demonstrate that the formation of meta-stable *γ*-MgH_2 under relatively mild conditions is achieved from a combination of ball-milling with LiCl and subsequent treatment with THF. The former treatment is extremely effective in reducing the hydride particle size while the latter appears to encourage *γ*-MgH_2 formation from the hydride THF adduct. Only by combining these two treatments does it appear possible to produce appreciable (>15 wt.%) *γ*-MgH_2 in the MgH_2 material. It is possible that during the hydrogen desorption process, *γ*-MgH_2 is first transformed into stable *β*-MgH_2 followed by dehydrogenation to Mg. The significant improvement in desorption performance of the *β-/γ*-MgH_2 nanocomposite over *β*-MgH_2 itself could be ascribed to two main factors: 1) a reactive, defective nanostructure which could lead to enhanced hydrogen diffusion and 2) an exothermic process associated with the *γ*- to *β*-MgH_2 transformation, resulting in improved hydrogen desorption kinetics.

Acknowledgments

The authors gratefully acknowledge financial support from the University of Glasgow and the National Natural Science Foundation of China (51571179). DHG also thanks the China Scholarship Council for the award of a scholarship to ZL.

References:

1 L. Schlapbach and A. Züttel, *Nature,* 2001, **414**, 353–358.
2 H. Reardon, J. M. Hanlon, R. W. Hughes, A. Godula-Jopek, T. K. Mandal and D. H. Gregory, *Energy Environ. Sci.,* 2012, **5**, 5951–5979.
3 H. Shao, G. Xin, J. Zheng, X. Li and E. Akiba, *Nano Energy,* 2012, **1**, 590–601.
4 R. Bardhan, A. M. Ruminski, A. Brand and J. J. Urban, *Energy Environ. Sci.,* 2011, **4**, 4882–4895.
5 W. Li, C. Li, H. Ma and J. Chen, *J. Am. Chem. Soc.,* 2007, **129**, 6710–6711.
6 Z. Dehouche, J. Goyette, T. Bose, J. Huot and R. Schulz, *Nano Letters,* 2001, **1**, 175–178.
7 C. An, G. Liu, L. Li, Y. Wang, C. Chen, Y. Wang, L. Jiao and H. Yuan, *Nanoscale,* 2014, **6**, 3223–3230.
8 C. S. Zhou, Z. G. Z. Fang, J. Lu and X. Y. Zhang, *J. Am. Chem. Soc.,* 2013, **135**, 10982–10985.
9 S. Er, G. A. de Wijs and G. Brocks, *J. Phys. Chem. Lett.,* 2010, **1**, 1982–1986.
10 K. J. Jeon, H. R. Moon, A. M. Ruminski, B. Jiang, C. Kisielowski, R. Bardhan and J. J. Urban, *Nature Mater.,* 2011, **10**, 286–290.
11 H. Imamura, M. Kusuhara, S. Minami, M. Matsumoto, K. Masanari, Y. Sakata, K. Itoh and T. Fukunaga, *Acta Mater.,* 2003, **51**, 6407–6414.
12 Y. S. Au, M. K. Obbink, S. Srinivasan, P. C. Magusin, K. P. de Jong and P. E. de Jongh, *Adv. Funct. Mater.,* 2014, **24**, 3604–3611.
13 M. Paskevicius, D. A. Sheppard and C. E. Buckley, *J. Am. Chem. Soc.,* 2010, **132**, 5077–5083.
14 A. Zaluska, L. Zaluski and J. O. Strom-Olsen, *J. Alloys Compd.,* 1999, **288**, 217–225.
15 G. Liang, J. Huot, S. Boily, A. Van Neste and R. Schulz, *J. Alloys Compd.,* 1999, **292**, 247–252.
16 M. Song, J.-L. Bobet and B. Darriet, *J. Alloys Compd.,* 2002, **340**, 256–262.
17 L. P. Ma, P. Wang and H. M. Cheng, *Int. J. Hydrogen Energy,* 2010, **35**, 3046–3050.
18 J. Lu, Y. J. Choi, Z. Z. Fang, H. Y. Sohn and E. Rönnebro, *J. Am. Chem. Soc.,* 2009, **131**, 15843–15852.
19 T. Liu, C. Qin, T. Zhang, Y. Cao, M. Zhu and X. Li, *J. Mater. Chem. A,* 2012, **22**, 19831–19838.
20 P. Vajeeston, P. Ravindran, M. Fichtner and H. Fjellvag, *J. Phys. Chem. C,* 2012, **116**, 18965–18972.
21 H. Shao, M. Felderhoff, F. Schuth and C. Weidenthaler, *Nanotechnology,* 2011, **22**.
22 R. Varin, T. Czujko and Z. Wronski, *Nanotechnology,* 2006, **17**, 3856.
23 M. Bortz, B. Bertheville, G. Böttger and K. Yvon, *J. Alloys Compd.,* 1999, **287**, L4–L6.
24 M. Ponthieu, F. Cuevas, J. F. Fernández, L. Laversenne, F. Porcher and M. Latroche, *J. Phys. Chem. C,* 2013, **117**, 18851–18862.
25 S. Cui, W. Feng, H. Hu, Z. Feng and Y. Wang, *Solid State Commun.,* 2008, **148**, 403–405.
26 A.C. Larson and R.B. vonDreele, *General Structure Analysis System (GSAS), Los Alamos National Laboratory Report LAUR*, pp. 86–748, Los Alamos, NM, USA, 1995.
27 B. H. Toby, *Journal of Applied Crystallography,* 2001, **34**, 210–213.
28 J. Huot, G. Liang, S. Boily, A. Van Neste and R. Schulz, *J. Alloys Compd.,* 1999, **293**, 495–500.
29 U. Wietelmann, A. Murso and S. Lang in *Lewis acid solutions in an oxygen donor-containing solvent or solvent mixture*, Google Patents, **2013**.
30 X. Wang and L. Andrews, *J. Phys. Chem. A,* 2004, **108**, 11511–11520.
31 J. M. Eyster and E. W. Prohofsky, *Spectrochim. Acta A* 1974, **30**, 2041-2046.
32 M. J. Michalczyk, *Organometallics,* 1992, **11**, 2307–2309.
33 M. Au, *J. Mater. Sci,* 2006, **41**, 5976–5980.
34 D. A. Sheppard, M. Paskevicius and C. E. Buckley, *J. Alloys Compd.,* 2010, **492**, L72–L74.
35 C. Ren, Z. Z. Fang, C. S. Zhou, J. Lu, Y. Ren, X. Y. Zhang and X. Y. Luo, *Int. J. Hydrogen Energy,* 2014, **39**, 5868–5873.
36 J. Graetz and J. J. Reilly, *J. Alloys Compd.,* 2006, **424**, 262–265.
37 H. E. Kissinger, *Analytical Chemistry,* 1957, **29**, 1702–1706.
38 L. Zhang, L. Chen, X. Xiao, X. Fan, J. Shao, S. Li, H. Ge and Q. Wang, *Int. J. Hydrogen Energy,* 2014, **39**, 12715–12726.